Scale Transition in Steel-Concrete Interaction. II: Applications

Roman Lackner[1] and Herbert A. Mang, F.ASCE[2]

Abstract: The proposed mode of consideration of the steel-concrete interaction (Part I) is applied to real-life engineering structures. Two structures recently investigated numerically at Vienna University of Technology are considered: (1) the reinforced concrete (RC) cooling tower III Ptolemaïs SES (Greece) and (2) a part of the shotcrete tunnel lining installed at the Lainzer tunnel (Austria). In both examples, the uniaxial fracture criterion used in Part I is replaced by the maximum stress (Rankine) criterion. Together with the Drucker-Prager criterion, which is used for the simulation of compressive failure of concrete/shotcrete, it defines the space of admissible stress states in the framework of multisurface plasticity. For the simulation of early-age fracture of shotcrete, consideration of the steel-concrete interaction presented in Part I of this paper is extended towards young shotcrete. Similar to the benchmark problem investigated in Part I of this paper, several analyses with different degrees of consideration of the steel-concrete interaction are performed. The obtained results give insight into the influence of the steel-concrete interaction on the load-carrying behavior of the investigated structures.

DOI: 10.1061/(ASCE)0733-9399(2003)129:4(403)

CE Database subject headings: Cooling towers; Concrete, reinforced; Collapse; Ultimate loads; Tunneling; Hybrid methods.

Analysis of Reinforced Concrete Cooling Tower Shell

This section refers to the application of the proposed mode of consideration of the steel-concrete interaction to the natural draught cooling tower III Ptolemaïs. This cooling tower is part of a 125 MW power station in Ptolemaïs, Greece. It was erected in 1964. Details concerning the geometric dimensions of the cooling tower, the material properties, the mode of reinforcement, and the type of loading can be found in Lackner and Mang (2001a).

Structural Model and Finite-Element Discretization

Because of the symmetry of the cooling tower and the loading conditions, only one half of the structure is considered in the analyses. For the discretization of the shell and the stiffening rings at the top and at the botton of the shell, 510 layered (thick) shell elements [element 75 of the *MARC* element library (*MARC* 1996)] are employed. Over the thickness, each element is divided into 13 layers. The thickness of layers representing the reinforcement is related to the cross-sectional area of the reinforcement per unit length. For the simulation of the columns, 30 beam elements are used.

[1]Research Assistant, Institute for Strength of Materials, Vienna Univ. of Technology, Karlsplatz 13/202, A-1040 Vienna, Austria. Email: Roman.Lackner@tuwien.ac.at

[2]Professor, Institute for Strength of Materials, Vienna Univ. of Technology, Karlsplatz 13/202, A-1040 Vienna, Austria. Email: Herbert.Mang@tuwien.ac.at

Note. Associate Editor: Franz-Josef Ulm. Discussion open until September 1, 2003. Separate discussions must be submitted for individual papers. To extend the closing date by one month, a written request must be filed with the ASCE Managing Editor. The manuscript for this paper was submitted for review and possible publication on December 17, 2001; approved on July 24, 2002. This paper is part of the ***Journal of Engineering Mechanics***, Vol. 129, No. 4, April 1, 2003. ©ASCE, ISSN 0733-9399/2003/4-403–413/$18.00.

Material Model for Reinforced Concrete

According to (*MARC* 1996), no stress component normal to the middle surface of the shell is considered in the element formulation of the layered (thick) shell element. In each layer, this stress component is set equal to zero. The remaining stress state consists of an in-plane stress state and two out-of-plane shear stresses. In the material model for concrete, the in-plane stress state and the out-of-plane shear stresses are treated separately. Whereas a multisurface plasticity model is used to control in-plane stresses, elastic degredation is considered for the description of the out-of-plane material response. As regards the description of the mechanical behavior of the reinforcement, a one-dimensional (1D) plasticity model is used. The stress state is reduced to one stress component. It refers to the direction of the steel bar.

One-Dimensional Material Model for Steel

The plasticity model used to control the stress component in the direction of the steel bar is given by

$$f_{\mathrm{RF}}(\sigma, q_{\mathrm{RF}}) = |\sigma| - \overline{q}_{\mathrm{RF}} \quad \text{with} \quad \overline{q}_{\mathrm{RF}} = f_{sy} - q_{\mathrm{RF}}(\alpha_{\mathrm{RF}}) \qquad (1)$$

where f_{sy} = yield stress; and σ = stress component in the direction of the reinforcement. q_{RF} and α_{RF} = steel strength and the strain-like internal variable, respectively. The model for the underlying hardening/softening behavior of cold-drawn steel is described in Part I of this series (Lackner and Mang 2003).

In-Plane Material Model for Concrete

For simulation of the mechanical behavior of concrete within one layer, a multisurface plasticity model is employed. It consists of the maximum stress (Rankine) criterion for the description of cracking and the Drucker-Prager criterion for the simulation of ductile failure of concrete under compressive loading (see Fig. 1).

Algorithmic difficulties arising from the nonsmoothness of the Rankine surface are circumvented by formulating the plasticity model in the principal stress space (Meschke 1996; Lackner et al. 2002). The basic requirements for use of this formulation, such as an isotropic stress-strain law and isotropic yield functions, are

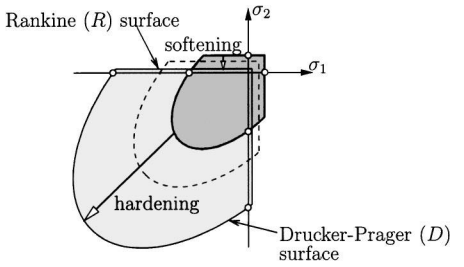

Fig. 1. Illustration of Drucker-Prager and Rankine yield criterion in 2D principal stress space

satisfied by the employed plasticity model. The space of admissible stress states is given in the principal stress space by (Fig. 1)

$$\boldsymbol{\sigma}=\begin{Bmatrix}\sigma_1\\ \sigma_2\end{Bmatrix}\in C_E \Leftrightarrow \begin{cases} f_{\mathrm{D}}(\sigma_1,\sigma_2,q_{\mathrm{D}})=\sqrt{J_2}+\kappa_{\mathrm{D}}I_1-\overline{q}_{\mathrm{D}}(\alpha_{\mathrm{D}})/\beta_{\mathrm{D}}\leqslant 0\\ f_{\mathrm{R},1}(\sigma_1,q_{\mathrm{R}})=\sigma_1-\overline{q}_{\mathrm{R}}(\alpha_{\mathrm{R}})\leqslant 0\\ f_{\mathrm{R},2}(\sigma_2,q_{\mathrm{R}})=\sigma_2-\overline{q}_{\mathrm{R}}(\alpha_{\mathrm{R}})\leqslant 0\end{cases} \tag{2}$$

with $\overline{q}_{\mathrm{D}}=f_{cy}-q_{\mathrm{D}}$; and $\overline{q}_{\mathrm{R}}=f_{tu}-q_{\mathrm{R}}$. f_{cy}=elastic limit under uniaxial compressive loading, with $f_{cy}=0.4f_{cu}$; and f_{tu}=tensile strength of concrete. q_{D} and q_{R} are the hardening/softening forces of the Drucker-Prager and the Rankine criterion, respectively. In Eq. (2), σ_1 and σ_2=principal stresses, with $\sigma_1\geqslant\sigma_2$; I_1 denotes the first invariant of the stress tensor; and J_2 stands for the second invariant of the stress deviator. β_{D} and κ_{D} are constant material parameters computed from the ratio between the biaxial compressive strength f_{cb} and the uniaxial compressive strength of concrete f_{cu}. The two respective stress states are given by $\boldsymbol{\sigma}=\lfloor 0, -f_{cu}\rfloor^T$ and $\boldsymbol{\sigma}=\lfloor -f_{cb}, -f_{cb}\rfloor^T$. Inserting these stress states in the Drucker-Prager criterion, one gets

$$f_{\mathrm{D}}=\frac{f_{cu}}{\sqrt{3}}-f_{cu}\kappa_{\mathrm{D}}-\frac{f_{cu}}{\beta_{\mathrm{D}}}=0 \quad \text{and} \quad f_{\mathrm{D}}=\frac{f_{cb}}{\sqrt{3}}-2\,f_{cb}\kappa_{\mathrm{D}}-\frac{f_{cu}}{\beta_{\mathrm{D}}}=0 \tag{3}$$

Based on a ratio between the biaxial and the uniaxial compressive strength of $f_{cb}/f_{cu}=1.16$, β_{D} and κ_{D} become 1.97 and 0.07, respectively.

The evolution of the plastic strain tensor $\boldsymbol{\varepsilon}^p$ and the hardening/softening variables α_{D} and α_{R} is based on an associate flow and hardening/softening rule, reading

$$\dot{\boldsymbol{\varepsilon}}^p=\begin{Bmatrix}\dot{\varepsilon}_1^p\\ \dot{\varepsilon}_2^p\end{Bmatrix}=\dot{\gamma}_{\mathrm{D}}\frac{\partial f_{\mathrm{D}}}{\partial\boldsymbol{\sigma}}+\dot{\gamma}_{R,1}\frac{\partial f_{\mathrm{R},1}}{\partial\boldsymbol{\sigma}}+\dot{\gamma}_{\mathrm{R},2}\frac{\partial f_{\mathrm{R},2}}{\partial\boldsymbol{\sigma}} \tag{4}$$

and

$$\dot{\alpha}_{\mathrm{D}}=\dot{\gamma}_{\mathrm{D}}\frac{\partial f_{\mathrm{D}}}{\partial q_{\mathrm{D}}}=\dot{\gamma}_{\mathrm{D}}\frac{1}{\beta_{\mathrm{D}}}, \quad \dot{\alpha}_{\mathrm{R}}=\dot{\gamma}_{\mathrm{R},1}\frac{\partial f_{\mathrm{R},1}}{\partial q_{\mathrm{R}}}+\dot{\gamma}_{\mathrm{R},2}\frac{\partial f_{\mathrm{R},2}}{\partial q_{\mathrm{R}}}=\dot{\gamma}_{\mathrm{R},1}+\dot{\gamma}_{\mathrm{R},2} \tag{5}$$

The nonlinear behavior of concrete under compressive loading is accounted for by a quadratic hardening function depicted in Fig. 2(a). The value of the internal variable α_{D} at peak strength, $\overline{\alpha}_{\mathrm{D}}$, is computed from the respective total strain ε^u under uniaxial loading. According to (CEB-FIP 1990), $\varepsilon^u=0.0022$. For the case of uniaxial loading

$$\overline{\alpha}_{\mathrm{D}}=\varepsilon^p=\varepsilon^u-\frac{f_{cu}}{E_c}=0.0022-\frac{f_{cu}}{E_c} \tag{6}$$

Similar to the crack criterion used in Part I of this paper, an exponential softening law is considered in the context of the Rankine criterion [see Fig. 2(b)]. The calibration of the softening

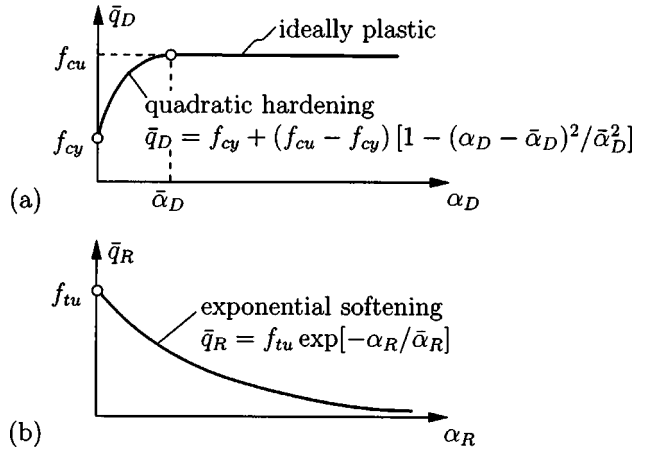

Fig. 2. Strain-hardening/softening considered in material model for concrete: (a) hardening in context of Drucker-Prager criterion and (b) softening in context of Rankine criterion

function follows the procedure outlined in Part I. The changing mode of reinforcement over the height of the shell is accounted for by distinguishing between nine different regions during calibration [see Lackner and Mang (2001a)]. Seven of them are located in different areas of the shell surface; the remaining two refer to the stiffening rings at the bottom and the top of the shell. The input parameters for the calibration procedure and the values obtained for the average crack spacing ℓ_s and the reduced average crack spacing ℓ_s^{red} can be found in (Lackner and Mang 2001a). The employed bond stress-bond slip relation is characterized by $s_1=0.6$ mm, $s_2=0.6$ mm, $s_3=1.0$ mm, $\tau_{\max}=2\sqrt{f_{cu}}$, $\tau_f=0.15\tau_{\max}$, and $\alpha=0.4$ (see Part I of this paper).

According to Part I of this paper, the calibration parameter $\overline{\alpha}_{\mathrm{R}}$ appearing in the softening function $\overline{q}_{\mathrm{R}}(\alpha_{\mathrm{R}})$ depicted in Fig. 2(b) is computed from the fracture energy G^f and the reduced average crack spacing ℓ_s^{red} as

$$\overline{\alpha}_{\mathrm{R}}=\frac{G^f}{\ell_s^{\mathrm{red}}f_{tu}} \tag{7}$$

Out-of-Plane Material Model for Concrete; Aggregate Interlock

If cracks are opening, the shear stiffness of concrete along the crack is reduced significantly. The residual interface shear transfer across cracks, resulting from the roughness of the crack face and from dowel action of the reinforcing bars, is considered by means of a decreasing out-of-plane shear modulus G_c, relating the out-of-plane shear stresses to the corresponding out-of-plane shear strains. A linear decrease of the out-of-plane shear modulus depending on the crack width $[\![u]\!]$ is employed (see, e.g., Cedolin and Dei Poli 1977; Meschke et al. 1999 for a similar approach):

$$G_c([\![u]\!])=0.25\frac{E_c}{2(1+\nu_c)}\left(1-\frac{[\![u]\!]}{[\![\overline{u}]\!]}\right) \tag{8}$$

where $[\![\overline{u}]\!]$=limiting value of $[\![u]\!]$. According to Cedolin and Dei Poli (1977), $[\![\overline{u}]\!]=0.75$ mm. For $[\![u]\!]\geqslant[\![\overline{u}]\!]$ aggregate interlock is neglected, i.e., $G_c=0$.

The crack width $[\![u]\!]$ in Eq. (8) is computed from the principal plastic strain ε_1^p and the reduced average crack spacing ℓ_s^{red}

$$[\![u]\!]=\langle\varepsilon_1^p\rangle\ell_s^{\mathrm{red}} \tag{9}$$

with $\langle\varepsilon_1^p\rangle=(\varepsilon_1^p+|\varepsilon_1^p|)/2$.

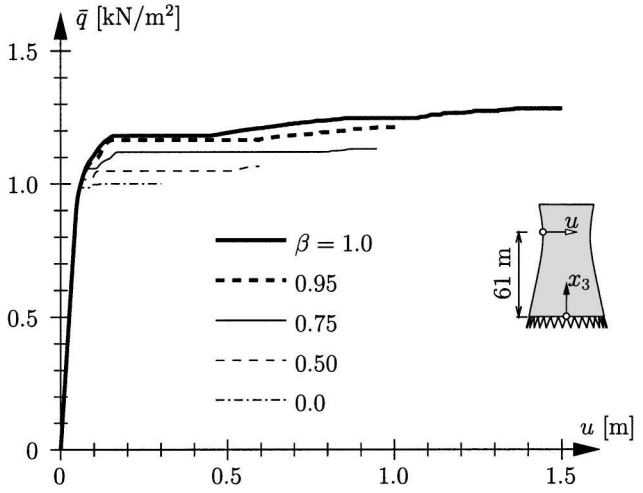

Fig. 3. Cooling tower: Load-displacement curves for different values of β

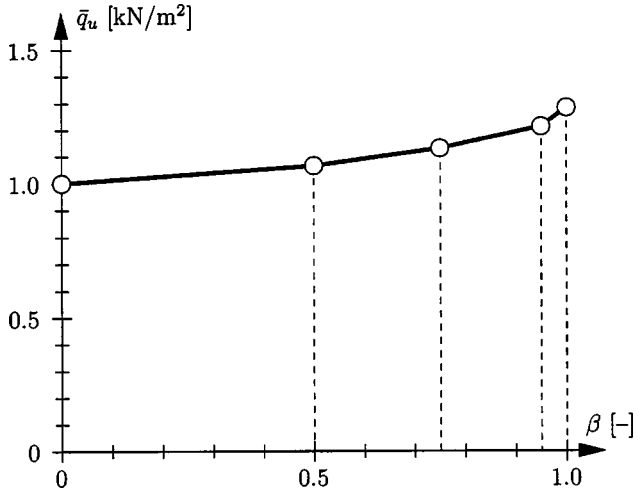

Fig. 4. Cooling tower: Collapse load $\overline{q_u}$ for different values of β

For closed cracks, characterized by $\sigma_1 < 0$ and $\alpha_R > 0$, where σ_1 denotes the maximum principal stress, the original shear transfer capacity cannot be recovered. The (reduced) out-of-plane shear modulus for closed cracks is given by

$$G_c = 0.25 \frac{E_c}{2(1+\nu_c)} \tag{10}$$

Numerical Analyses

Similar to the benchmark problem considered in Part I of this paper, the influence of tension stiffening on the load-carrying behavior is investigated by means of the dimensionless parameter β. $\beta = 1$ in case of full consideration of the tension stiffening effect, whereas in case of $\beta = 0$, tension stiffening is neglected. The calibration parameter of the Rankine criterion [see Eq. (7)] becomes

$$\overline{\alpha}_R = \frac{G^f}{[(1-\beta)\ell_s + \beta \ell_s^{\text{red}}] f_{tu}} \tag{11}$$

Fig. 3 shows the load-displacement curves obtained for different values of β. u = radial displacement component of a shell point located 61 m above the bottom ring at $\Theta = 0°$, i.e., at the windward meridian of the cooling tower. For $\beta = 1$, i.e., for full consideration of tension stiffening, displacements up to 1.5 m were obtained at the collapse load. The collapse of the cooling tower is caused by vanishing stiffness (characterized by a horizontal slope of load-displacement curves at the collapse load $\overline{q_u}$). In the finite-element (FE) analysis, collapse of the cooling tower is assumed when the Newton-Raphson iteration employed in the context of incremental-iterative FE analyses does not converge. For reduced consideration of tension stiffening $\beta < 1$, vanishing of the stiffness is still responsible for the collapse of the shell. However, the displacement at which structural failure occurs decreases with decreasing values of β.

The effect of tension stiffening on the collapse load is illustrated in Fig. 4. Disregard of tension stiffening ($\beta = 0$) gives the smallest collapse load. For increasing values of β, an increase of the collapse load is observed. Finally, for full consideration of tension stiffening ($\beta = 1$), an increase of the collapse load by almost 30% is obtained.

The influence of tension stiffening on the collapse load was already pointed out by Floegl and Mang (1982). It is a direct consequence of the increase of the stiffness of the structure resulting in a change of the load-carrying behavior. For the cooling tower shell considered, this is illustrated by the distribution of the hardening/softening variable α_R of the outer layer of the shell (Fig. 5). For $\beta = 0$, i.e., in case of disregard of tension stiffening, intensive cracking of concrete is observed in the upper half of the cooling tower. Failure is initiated at the windward side of the cooling tower. For increasing values of β, the increase of stiffness results in a distribution of cracks along the windward meridian of the shell. In case of full consideration of tension stiffening, cracks are almost reaching the stiffening ring at the bottom of the shell. Apparently, the change in the distribution of cracks is a consequence of the change in the load-carrying behavior. As stated earlier, the latter is the main reason for the increase of the collapse load observed by Floegl and Mang (1982) and in the analysis of the cooling tower.

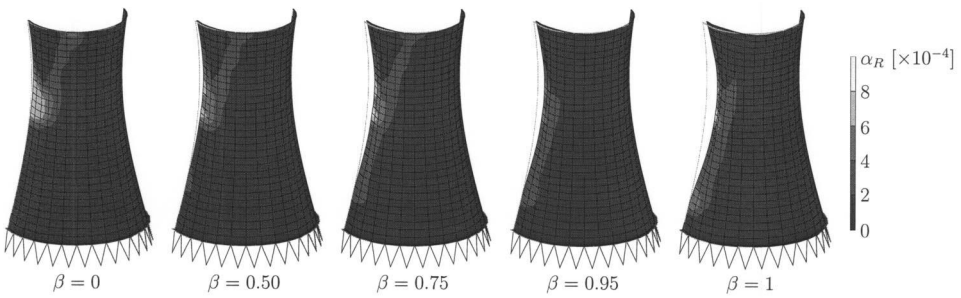

Fig. 5. Cooling tower: Distribution of internal variable α_R in outer layer of shell for different values of β at respective collapse loads

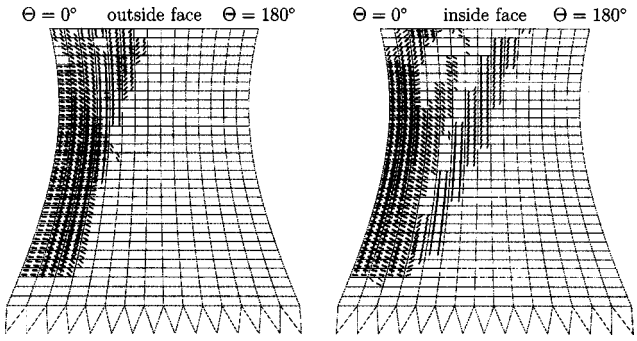

Fig. 6. Cooling tower: Crack pattern on outside and inside face at $\overline{q_u}$ obtained from analysis with $\beta = 1$

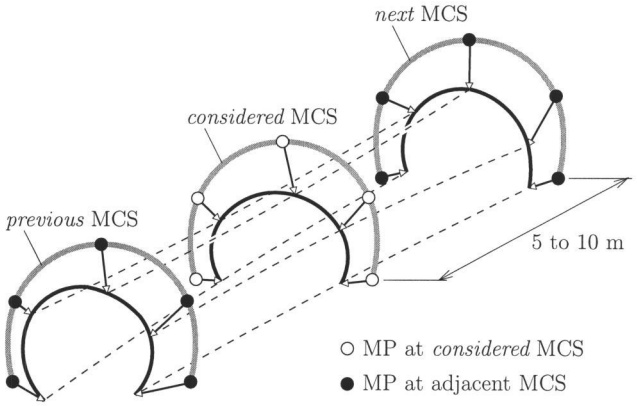

Fig. 7. Illustration of interpolation of displacements between measurement points

Fig. 6 shows the crack distribution on the outside and inside face of the shell at the collapse load obtained from the analysis characterized by full consideration of tension stiffening. The wind load leads the axial tensile forces at the windward meridian of the cooling tower, causing the opening of horizontal membrane cracks reaching from the outside to the inside face of the shell. The bending of the shell results in aligned meridional cracks on both sides of the shell. For both membrane and bending cracking a distribution of cracks over more rows of finite elements is observed. This observation supports the basic assumption of Part I, stating that the reinforcement leads to cracking of every element intersected by the reinforcement bars and located in regions where tensile loading is applied.

Analysis of Shotcrete Tunnel Lining

In this section, the presented mode of consideration of the steel-concrete interaction is applied to shotcrete linings which constitute the primary support when driving tunnels according to the New Austrian Tunneling Method (NATM). Shotcrete is applied onto the tunnel wall right after the excavation of a new stretch of the tunnel, finally forming a thin, flexible lining. For the analyses of shotcrete linings, hybrid analysis schemes became rather popular over the last few years (Zachow 1995; Rokahr and Zachow 1997; Hellmich et al. 1999a; Lackner and Mang 2001c). They represent a combination of measurements of in situ displacement and of a constitutive model for shotcrete.

Hybrid Analyses of Tunnel Linings

In NATM tunneling, 3D displacement vectors at discrete points, so-called measurement points (MPs), located on the inner surface of the lining are continuously measured. MPs are arranged in measurement cross sections (MCSs) (see Fig. 7). The displacement vectors of these points are updated once a day. They serve as input for hybrid analyses of tunnel linings. For the numerical simulations, however, a continuous displacement field in both space and time is required. Fig. 7 illustrates the spatial interpolation of measured 3D displacement vectors providing a continuous displacement field in space. In general, polynomial functions are used for this purpose. Continuity of the displacement field with respect to time is obtained from linear interpolation between the time instants at which the measurements were performed. Finally, the displacement field at the inner surface of the lining is given as

$$\overline{\mathbf{u}}(s,z;t) = \begin{Bmatrix} \overline{u_x}(s,z;t) \\ \overline{u_y}(s,z;t) \\ \overline{u_z}(s,z;t) \end{Bmatrix} \tag{12}$$

where s and z = the coordinate in the circumferential and longitudinal direction of the tunnel, respectively. According to Lackner and Mang (2001c), the displacement vector $\mathbf{u}$ of any point of the shotcrete lining can be computed directly from the displacement field at the inner surface of the lining, $\overline{\mathbf{u}}$, by assuming that

- The thickness of the lining remains constant during deformation, and
- Lines which are perpendicular to the inner surface of the lining at the beginning of the analysis remain perpendicular to the inner surface during deformation.

In view of the geometric dimensions of the lining (thin shell), both assumptions seem to be reasonable. Fig. 8 illustrates this approach for a point of the lining given by its coordinates in the circumferential, radial, and longitudinal direction (s,ζ,z). It is noted that in contrast to the hybrid methods described in Zachow (1995); Rokahr and Zachow (1997); Hellmich et al. (1999a), no FE analysis is required. The displacement field is obtained from interpolation between MPs and geometrical considerations as depicted in Fig. 8.

Determination of Strains from Displacement Field

Hybrid analyses of tunnel linings are performed for each MCS separately. In order to account for deformations in the longitudinal direction of the tunnel, displacements at MCSs adjacent to the *considered* MCS, referred to as *previous* and *next* MCS, are required (Fig. 7). Since shotcrete linings are mainly loaded biaxially, i.e., in the circumferential and in the longitudinal direction of the tunnel, only two strain components are considered in the following (Lackner and Mang 2001c):

1. The axial strain in the longitudinal direction can be computed from

$$\varepsilon_z(s,\zeta;t) = \left.\frac{\partial u_z(s,\zeta,z;t)}{\partial z}\right|_{z=0} \tag{13}$$

where $z = 0$ = the location of the *considered* MCS. Since the change in the curvature in the longitudinal direction is negligible, ε_z is assumed to be constant over the thickness of the lining. The respective constant value for ε_z is determined for a section of the lining from the displacement field of the

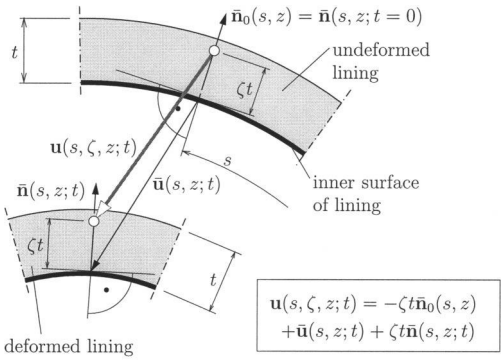

Fig. 8. Determination of displacement field $\mathbf{u}(s,\zeta,z;t)$ from given displacement field at inner surface of lining, $\bar{\mathbf{u}}(s,z;t)$

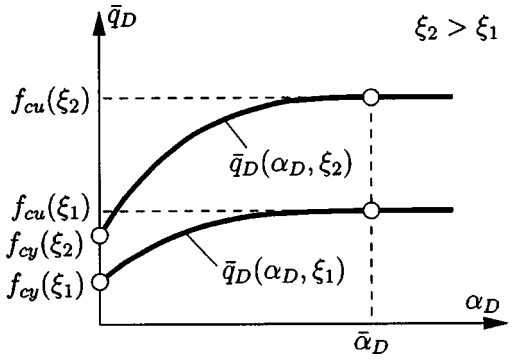

Fig. 10. Material model for shotcrete: Increase of $\bar{q}_D$ in consequence of microcracking (strain hardening) for two different values of ξ

inner surface of the lining:

$$\varepsilon_z(s;t)=\varepsilon_z(s,\zeta=0;t)=\left.\frac{\partial\bar{u}_z(s,z;t)}{\partial z}\right|_{z=0} \tag{14}$$

2. The axial strain in the circumferential direction ε_φ is computed by means of layered beam elements (Fig. 9). Based on the known displacement field $\mathbf{u}(s,\zeta,z;t)$, the length of each layer of the beam element can be computed. The obtained length is used for determination of the circumferential strain ε_φ of the kth layer in the form

$$\varepsilon_{\varphi,k}=\frac{\ell_k(t)-\ell_k(t=0)}{\ell_k(t=0)} \tag{15}$$

Determination of Stresses from Strains–Material Model for Shotcrete

Shotcrete linings are surface structures which, by definition, are mainly loaded in the circumferential and longitudinal direction of the tunnel. Accordingly, a plane-stress situation is assumed in each layer of the previously mentioned beam element. For determination of the axial stress components σ_φ and σ_z from the axial strain components ε_φ and ε_z, a thermochemomechanical material model for shotcrete is employed (Hellmich et al. 1999b; Sercombe et al. 2000; Lackner et al. 2002). It accounts for

- The hydration process, i.e., the chemical reaction between cement and water: It results in increasing stiffness (aging elasticity) and strength (chemical hardening) as well as chemical shrinkage. The reaction extent is described by means of the degree of hydration ξ which is defined by the ratio of the current specific mass of water bound in hydrates m and the respective mass at complete hydration m_∞,
- Microcracking,
- Short-term creep which stems from stress-induced movements of water in the capillary pores of concrete (Ruetz 1966; Wittmann 1982; Ulm 1998), and
- Long-term or flow creep which follows from dislocationlike processes in the nanopores of cement gel (Wittmann 1982).

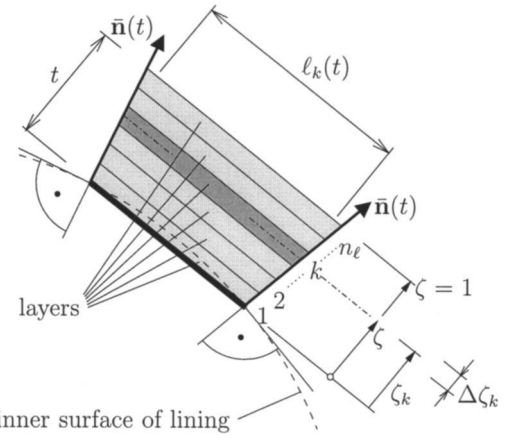

Fig. 9. Determination of circumferential strain in tunnel lining by means of layered beam element

For the simulation of microcracking, the same set of yield surfaces as used in the cooling tower analysis is employed. In the present analysis, however, the principal stresses σ_1 and σ_2 are replaced by the axial stress in the circumferential and longitudinal direction σ_φ and σ_z. The respective yield functions define the space of admissible stress states in the form

$$\boldsymbol{\sigma}=\begin{Bmatrix}\sigma_\varphi\\ \sigma_z\end{Bmatrix}$$

$$\in C_E\Leftrightarrow\begin{cases} f_D(\sigma_\varphi,\sigma_z,q_D)=\sqrt{J_2}+\kappa_D I_1-\bar{q}_D(\alpha_D,\xi)/\beta_D\leqslant 0\\ f_{R,\varphi}(\sigma_\varphi,q_{R,\sigma})=\sigma_\varphi-\bar{q}_{R,\varphi}(\alpha_{R,\varphi},\xi)\leqslant 0\\ f_{R,z}(\sigma_z,q_{R,z})=\sigma_z-\bar{q}_{R,z}(\alpha_{R,z},\xi)\leqslant 0\end{cases} \tag{16}$$

where $\bar{q}_D=f_{cy}-q_D=$ compressive strength; and $\bar{q}_{R,\varphi}=f_{tu}-q_{R,\varphi}$ and $\bar{q}_{R,z}=f_{tu}-q_{R,z}=$ tensile strengths in the circumferential and longitudinal direction of the tunnel, respectively. In contrast to the plasticity model used in the cooling tower analysis, $\bar{q}_D$ as well as $\bar{q}_{R,\varphi}$ and $\bar{q}_{R,z}$ depend on both the respective hardening/softening variable α and the extent of the hydration represented by ξ (chemomechanical coupling).

For the Drucker-Prager criterion, quadratic hardening of the compressive strength is considered (Fig. 10). Similar to the concrete model used in the cooling tower analysis [Eq. (6)], the calibration parameter $\bar{\alpha}_D$ is obtained as

$$\bar{\alpha}_D=0.0022-\frac{f_{cu,\infty}}{E_{c,\infty}} \tag{17}$$

where $f_{cu,\infty}$ and $E_{c,\infty}=$ final values of the uniaxial compressive strength and Young's modulus, respectively.

During the chemical reaction of concrete, new hydrates are formed in a state which is free of microstress (Bažant 1979). Hence, each hydrate is exclusively loaded by microstress resulting from macrostress applied *after* the formation of the respective hydrate (Fig. 11). The formation of new hydrates results in an

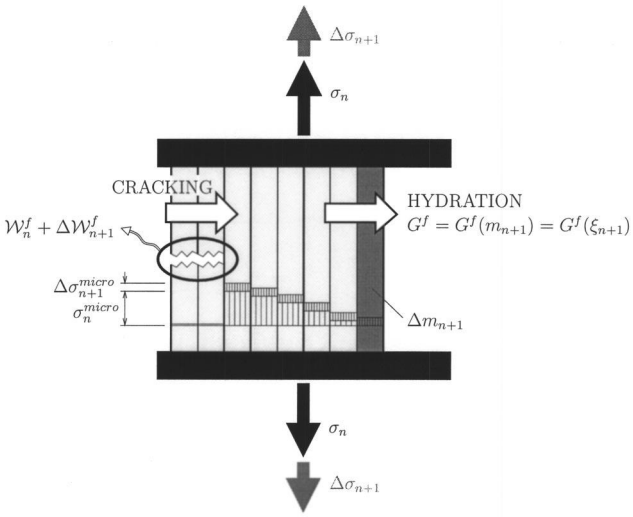

Fig. 11. 1D rheological model illustrating formation of new hydrates in state which is free of microstress and cracking of hydrates

increase of the tensile strength (chemical hardening). On the other hand, the cracking of shotcrete characterized by the fracture of hydrates leads to a reduction of the tensile strength (strain softening). In order to account for both chemical hardening and strain softening, the incremental update of the tensile strength $\bar{q}_R$ within, e.g., the $(n+1)$-st load increment is proposed as follows (Fig. 12):

$$\Delta\bar{q}_{R,n+1} = \left[\bar{q}_{R,n} + \underbrace{\Delta\bar{q}_{R,n+1}^{hyd}(\Delta\xi_{n+1})}_{\text{chemical hardening}}\right]\left[1 - \underbrace{\exp\left(-\frac{\Delta\alpha_{R,n+1}}{\bar{\alpha}_{R,n+1}}\right)}_{\text{strain softening}}\right] \tag{18}$$

where $\Delta\bar{q}_{R,n+1}^{hyd}$ = increase of tensile strength in the $(n+1)$-st time increment in consequence of chemical hardening. It is computed from the incremental increase of the degree of hydration, $\Delta\xi_{n+1}$.

At fracture, the hydrates are loaded by microstresses (Fig. 11). This results in a macroscopically observable energy release, denoted as $\mathcal{W}^f$. The amount of released energy related to the cracking of all hydrates located in a unit area of the crack surface is the fracture energy G^f. The increase of G^f in the course of the hydration process (De Schutter and Taerwe 1997; Lackner and Mang 2001b) is considered by relating the calibration parameter $\bar{\alpha}_{R,n+1}$ in Eq. (18) to the difference between the fracture energy of the hydrates formed so far, $G^f(\xi_{n+1})$, and the energy released by cracking in previous time increments, $\mathcal{W}_n^f$, giving

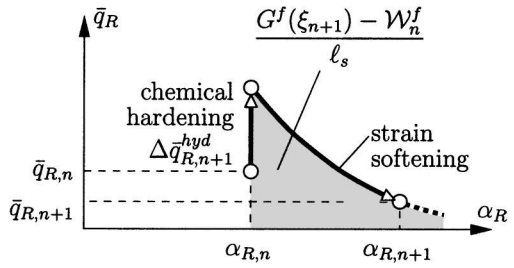

Fig. 12. Material model for shotcrete: Illustration of incremental change of $\bar{q}_R$ for the $(n+1)$-st time increment consisting of chemical hardening and strain softening

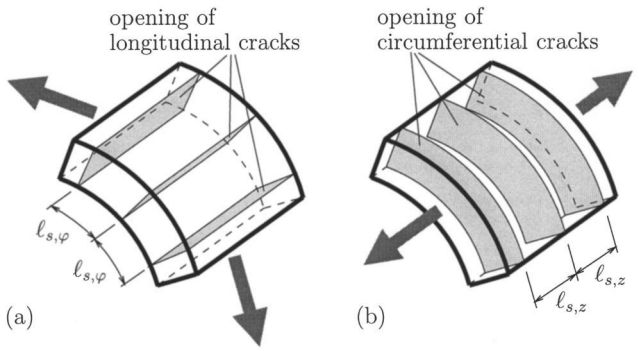

Fig. 13. Material model for reinforced shotcrete: Illustration of cracks opening in shotcrete lining with average crack spacing in (a) circumferential and (b) longitudinal direction

$$\frac{G^f(\xi_{n+1}) - \mathcal{W}_n^f}{\ell_s(\xi_{n+1})} = \int_{\alpha_{R,n}}^{\infty} [\bar{q}_{R,n} + \Delta\bar{q}_{R,n+1}^{hyd}(\Delta\xi_{n+1})] \times \exp\left(-\frac{\Delta\alpha_{R,n+1}}{\bar{\alpha}_{R,n+1}}\right) d\alpha_R \tag{19}$$

In Eq. (19), $\ell_s(\xi)$ = average crack spacing which, in case of early-age shotcrete, is a function of the extent of the hydration process. Integration of Eq. (19) gives the calibration parameter $\bar{\alpha}_R$ for the $(n+1)$-st time increment

$$\bar{\alpha}_{R,n+1} = \left[\sum_{i=1}^{n+1} \Delta G^f(\Delta\xi_i) - \mathcal{W}_n^f\right] \times \frac{1}{[\bar{q}_{R,n} + \Delta\bar{q}_{R,n+1}^{hyd}(\Delta\xi_{n+1})]\ell_s(\xi_{n+1})} \tag{20}$$

where $G^f(\xi_{n+1})$ was replaced by the incremental changes of the fracture energy, with

$$G^f(\xi_{n+1}) = \sum_{i=1}^{n+1} \Delta G^f(\Delta\xi_i) \tag{21}$$

The calibration parameter $\bar{\alpha}_{R,n+1}$ given in Eq. (20) is determined for the Rankine criterion formulated for the axial stress component in the circumferential and the longitudinal direction of the tunnel. Consideration of two yield functions, $f_{R,\varphi}$ and $f_{R,z}$, in the context of the employed multisurface plasticity model for shotcrete allows us to treat cracking in the circumferential and longitudinal direction as two independent processes.

Steel–Concrete Interaction of Early-Age Shotcrete

The presence of reinforcement in shotcrete linings leads to the distribution of cracks finally forming a stabilized crack pattern (Fig. 13). For determination of the average crack spacing ℓ_s and the reduced average crack spacing ℓ_s^{red}, the procedure outlined in Part I of this paper is employed. These quantities are computed for different values of ξ, i.e., for different stages of the hydration process. For this purpose, the nonlinear bond slip-bond stress relation used in Part I is extended towards aging materials (Fig. 14). Unfortunately, experimental data on the steel-concrete interaction of early-age shotcrete/concrete are rather rare. Results of pull-out experiments of specimens characterized by different age and embedment length are reported in Chapman and Shah (1987). Fig. 14(a) contains the obtained maximum bond stress τ_{max} for differ-

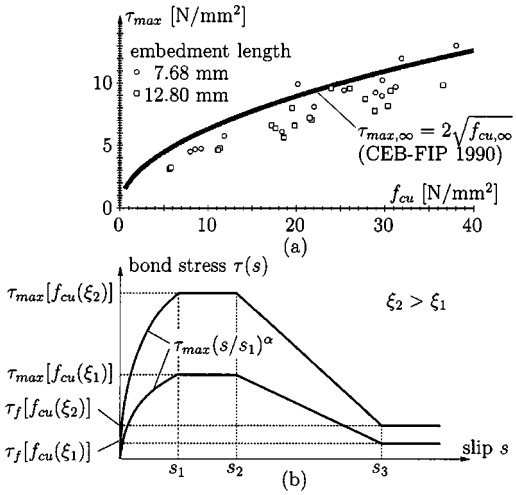

Fig. 14. Material model for reinforced shotcrete: (a) $\tau_{max}-f_{cu}$ pairs obtained from pull-out experiments for different ages of concrete (Chapman and Shah 1987) and (b) proposed extension of bond slip–bond stress relation given in Part I of this paper to consideration of aging

ent values of the uniaxial compressive strength f_{cu}, i.e., for different ages of the investigated concrete. In addition, the relation between the maximum bond stress and the uniaxial compressive strength at complete hydration, i.e., between $\tau_{\max,\infty}$ and $f_{cu,\infty}$, according to CEB-FIP (1990) is plotted. Even though this relation accounts for different types of concrete characterized by different values of the uniaxial compressive strength, good agreement between this relation and the experimental results of Chapman and Shah (1987) is observed. This observation was the basis for the extension of the $\tau_{\max,\infty}-f_{cu,\infty}$ relation given in CEB-FIP (1990) to early-age shotcrete/concrete in the form [Fig. 14(b)]

$$\tau_{\max,\infty}=2\sqrt{f_{cu,\infty}} \Rightarrow \tau_{\max}[f_{cu}(\xi)]=2\sqrt{f_{cu}(\xi)} \tag{22}$$

Furthermore, the experimental results of Chapman and Shah (1987) indicate that the influence of the age of concrete on the value of bond slip at maximum bond stress is small. Hence, the slip values s_1 to s_3 which define the underlying bond stress–bond slip relation in Fig. 14(b) are assumed to be constant during hydration. Similar to the determination of $\overline{\alpha}_D$ in Eq. (17), their (constant) values are related to the material properties of shotcrete at complete hydration.

The bond stress–bond slip relation given in Fig. 14(b) serves as input for determination of ℓ_s and ℓ_s^{red}. As proposed in Part I of this paper, tension stiffening is considered within the calibration of the fracture criterion. Accordingly, the incremental change of the fracture energy, ΔG^f, appearing in Eq. (20) is increased by the ratio $\ell_s/\ell_s^{\text{red}}$, giving

$$\overline{\alpha}_{R,n+1}=\left[\sum_{i=1}^{n+1}\frac{\ell_s(\xi_i)}{\ell_s^{\text{red}}(\xi_i)}\Delta G^f(\Delta\xi_i)-\mathcal{W}_n^f\right] \times\frac{1}{[\overline{q}_{R,n}+\Delta\overline{q}_{R,n+1}^{\text{hyd}}(\Delta\xi_{n+1})]\ell_s(\xi_{n+1})} \tag{23}$$

Hybrid Analyses of Lainzer Tunnel

For the analysis of the Lainzer tunnel, the MCS of Track 9 located at km 8.340 was chosen. For evaluation of the axial strains in the longitudinal direction, the *previous* and the *next* MCS at km 8.331 and km 8.350 were used.

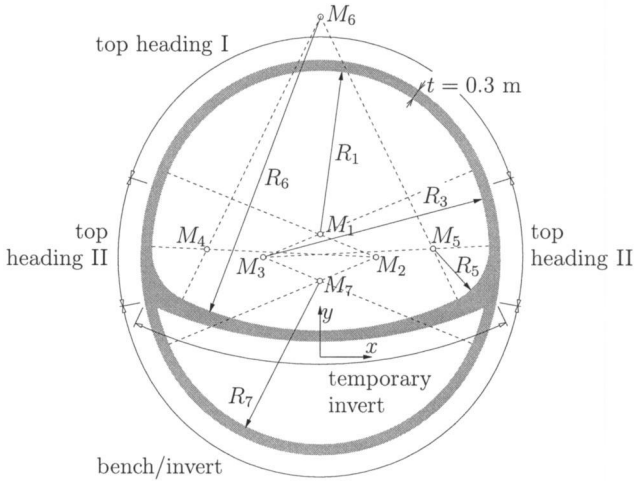

Fig. 15. Lainzer tunnel—Bierhäuselberg: cross section

Table 1. Lainzer Tunnel—Bierhäuselberg∷ Geometric Properties of Cross Section

Number	Center Point x (m)	Center Point y (m)	Radius R (m)
1	0	3.40	4.74
2	1.52	2.77	6.39
3	−1.52	2.77	6.39
4	−3.06	3.00	1.50
5	3.06	3.00	1.50
6	0	9.30	8.50
7	0	2.14	4.44

Table 2. Lainzer Tunnel: Material Properties for Shotcrete

Final Young's modulus $E_{c,\infty}$ (N/mm²)	40,800
Poisson's ratio ν_c (-)	0.2
Final compressive strength $f_{cu,\infty}$ (N/mm²)	39.6
Tensile strength f_{tu}	$f_{cu}/10$

Geometric Dimensions and Material Properties

The standard cross section of the Lainzer tunnel is shown in Fig. 15. The geometric properties of this cross section are given in Table 1.

Typical mechanical properties of shotcrete used in the following analyses are listed in Table 2. The value of the fracture energy G^f at complete hydration G_∞^f is computed from (CEB-FIP 1990)

$$G_\infty^f=G_0^f\left(\frac{f_{cu,\infty}}{f_{cu,0}}\right)^{0.7}. \tag{24}$$

where $f_{cu,0}=10$ N/mm². G_0^f depends on the maximum aggregate size $d_{\max}$. For the maximum aggregate size of shotcrete, which is 8 mm, G_0^f is obtained as 0.025 Nmm/mm² (CEB-FIP 1990), giving $G_\infty^f=0.065$ Nmm/mm².

The shotcrete lining is reinforced with two layers of AQ60 (∅6 mm, spacing of 100 mm, giving $a_s=283$ mm²/m). The shotcrete cover c is equal to 30 mm. According to CEB-FIP (1990), the effective tensile height of shotcrete is obtained as

$$h_{c,\text{eff}}=\min\{2.5(c+\varnothing_s/2),t/2\}=\min\{2.5(30+6/2),300/2\} =82.5\text{ mm} \tag{25}$$

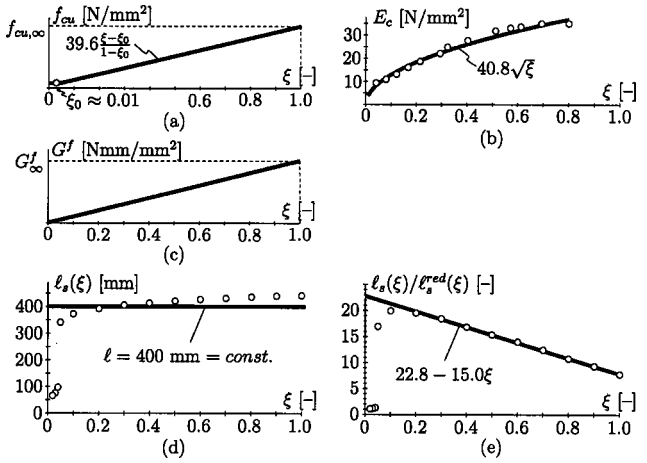

Fig. 16. Lainzer tunnel: Material functions for (a) f_{cu}, (b) E_c, and (c) G^f; (d) average crack spacing ℓ_s, and (e) ratio of average crack spacing and reduced average crack spacing, $\ell_s/\ell_s^{\text{red}}$, obtained from application of calibration procedure outlined in Lackner and Mang (2003)

For determination of the average crack spacing ℓ_s and the reduced average crack spacing ℓ_s^{red}, the procedure proposed in Lackner and Mang (2003) is performed for different stages of the hydration process. The employed bond stress–bond slip relation is defined by $\tau_{\max}[f_{cu}(\xi)]=2\sqrt{f_{cu}(\xi)}$, $\tau_f[f_{cu}(\xi)]=0.15\tau_{\max}[f_{cu}(\xi)]$, $s_1=s_2=0.6$ mm, $s_3=1.0$ mm, and $\alpha=0.4$. Determination of ℓ_s and ℓ_s^{red} for a certain stage of the hydration process is based on the respective bond stress–bond slip relation and the respective values of the uniaxial compressive strength f_{cu}, Young's modulus E_c, and the fracture energy G^f [see Figs. 16(a–c)]. The obtained discrete values for the average crack spacing ℓ_s and the ratio of the average crack spacing and the reduced average crack spacing, $\ell_s/\ell_s^{\text{red}}$, are given by the circles in Figs. 16(d and e). The obtained relations are approximated by a constant and a linear function, respectively. Both functions serve as input for the numerical analysis of the tunnel lining.

Construction History

Fig. 17 shows the construction history for the "Bierhäuselberg" tunnel containing Track 9. The reference time $t=0$ is defined as the time instant at the beginning of construction at the *considered* MCS. For the "Bierhäuselberg" tunnel, the reference time refers to the excavation of the Top Heading I, which took place on January 23, 2001 at km 8.340 of Track 9. 370 h after the erection of Top Heading I the excavation was interrupted for almost 69 days.

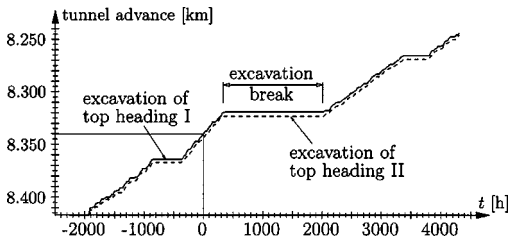

Fig. 17. Lainzer tunnel (km 8.340): Construction history of "Bierhäuselberg" tunnel containing Track 9

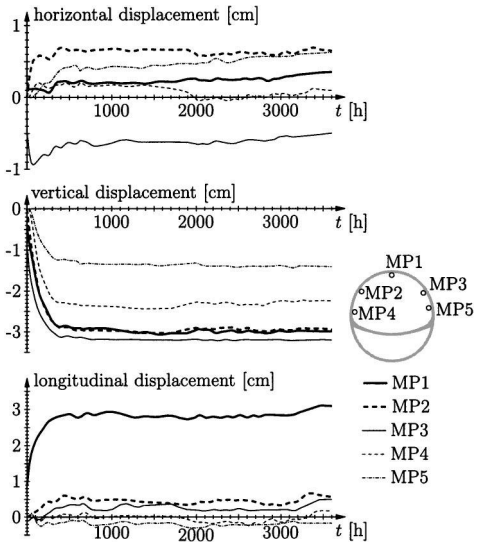

Fig. 18. Lainzer tunnel (km 8.340): Displacement history of measurement points at *considered* measurement cross sections

Displacement Measurements

Five measurement devices were installed at each MCS of the Lainzer tunnel. Fig. 18 contains the displacement histories of the MPs of the *considered* MCS. The displacements are increasing rapidly during the first 300 to 400 h. Actually, settlements up to 3 cm forced the construction company to stop the excavation at $t=370$ h. During the construction break, the footings of the existing Top Heading II were improved by installing micropiles of 80 mm diameter. After this improvement, the settlements did not increase further. Even after continuation of the excavation work, the displacements of the *considered* MCS remained almost unchanged.

Numerical Results

The finite beam elements employed in the hybrid analysis of the *considered* MCS were divided into six layers of 5 cm thickness each. At the interface between Top Heading I and Top Heading II, hinged conditions were assumed.

In order to assess the influence of tension stiffening on the loading of the lining, the calibration of the Rankine criterion (23) was adapted as

$$\overline{\alpha}_{\text{R},n+1}=\left[\sum_{i=1}^{n+1}\frac{\ell_s(\xi_i)}{(1-\beta)\ell_s(\xi_i)+\beta\ell_s^{\text{red}}(\xi_i)}\Delta G^f(\Delta\xi_i)-\mathcal{W}_n^f\right]\times\frac{1}{[\overline{q}_{\text{R},n}+\Delta\overline{q}^{\text{hyd}}_{\text{R},n+1}(\Delta\xi_{n+1})]\ell_s(\xi_{n+1})} \tag{26}$$

where β = dimensionless parameter which was also used in the preceding example.

Figs. 19 and 20 show the history of the axial force in the circumferential and the longitudinal direction, computed from

$$n_\varphi=\sum_{k=1}^{n_\ell}\sigma_{\varphi,k}h\Delta\zeta_k \quad\text{and}\quad n_z=\sum_{k=1}^{n_\ell}\sigma_{z,k}h\Delta\zeta_k \tag{27}$$

respectively, at the footings of Top Heading I of the *considered* MCS. The obtained histories are characterized by an oscillating behavior of the axial forces between -3 and $+1$ MN/m. This type of behavior reflects the oscillating measurement values shown in the displacement histories obtained from the construction site

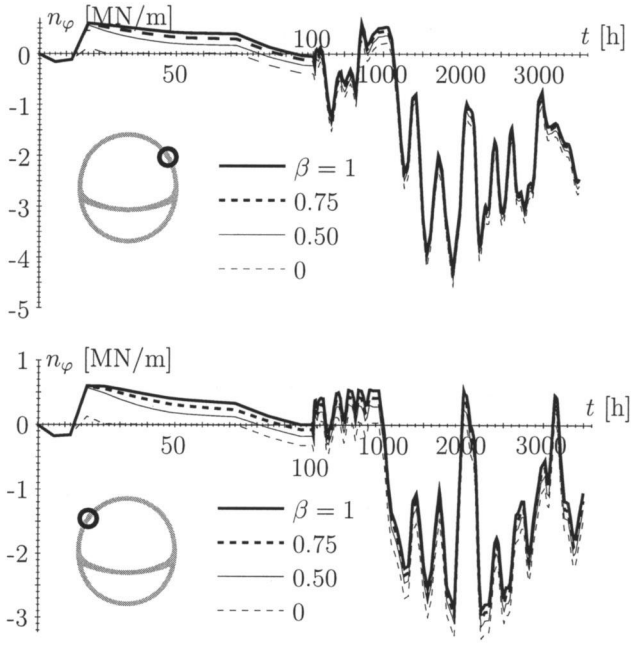

Fig. 19. Lainzer tunnel (km 8.340): History of axial force in circumferential direction

(Fig. 18). In both the circumferential and the longitudinal direction, tensile loading of the lining starts at $t \approx 10$ h. This time instant refers to the onset of chemical shrinkage. Moreover, the maximum temperature in the shotcrete lining during hydration is reached 10 h after installation (Lackner and Mang 2002b). Hence, in addition to chemical shrinkage, cooling of the lining causes an increase of tensile loading for $t > 10$ h. A strong influence of tension stiffening is observed during the first 100 h after installation of Top Heading I. This time span is characterized by the aforementioned tensile loading. Tension stiffening results in a delay of strain softening caused by cracking. For the remaining simulation time, i.e., for $t > 100$ h, the distance between the histories of axial

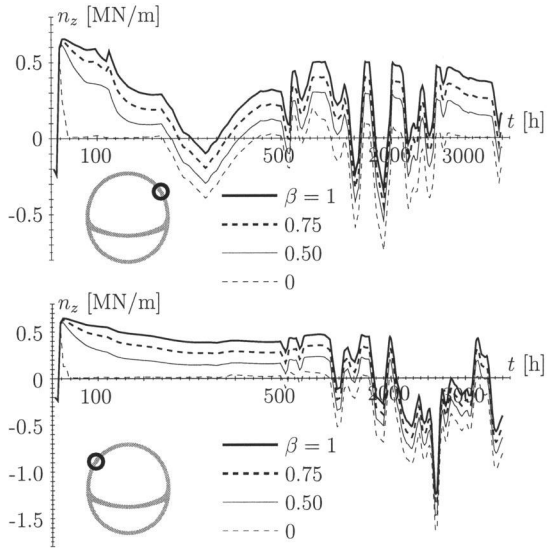

Fig. 20. Lainzer tunnel (km 8.340): history of axial force in longitudinal direction

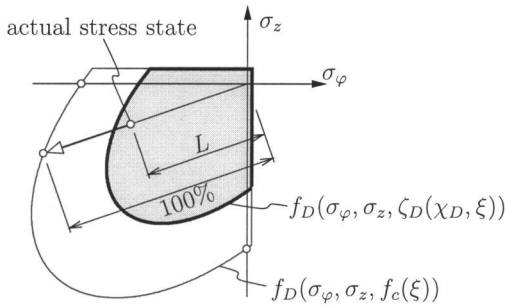

Fig. 21. Illustration of level of loading L in $\sigma_\varphi - \sigma_z$ stress space

forces corresponding to different levels of consideration of tension stiffening, i.e., to different values of β, remains almost unchanged.

The level of loading L serves as a safety measure for shotcrete tunnel linings. It amounts to 0% for the unloaded structure and to 100% when the uniaxial compressive strength f_{cu} is reached. For the Drucker-Prager criterion, the level of loading for the *k*th layer is given as (Fig. 21)

$$L_k = \frac{\sqrt{J_2(\sigma_{\varphi,k}, \sigma_{z,k})} + \kappa_D I_1(\sigma_{\varphi,k}, \sigma_{z,k})}{f_{cu}(\xi_k)/\beta_D} \tag{28}$$

Fig. 22 shows the evolution of the maximum of $\overline{L}$ in the *considered* MCS, where

$$\overline{L} = \sum_{k=1}^{n} L_k \Delta\zeta_k \tag{29}$$

The value of $\overline{L}_{\max}$ ranges between 15 and 50%. The influence of tension stiffening on the evolution of $\overline{L}_{\max}$ is marginal. In contrast to the cooling tower where tension stiffening resulted in a change in the load-carrying behavior of the shell, the increased stiffness from tension stiffening has no influence on the deformation state of the lining. The deformations are obtained from measurements performed at the construction site and spatial interpolation as outlined in this paper.

Conclusions

In this paper, applications of the proposed consideration of steel-concrete interaction to real-life engineering structures were presented. From the obtained numerical results, the following conclusions can be drawn:

- In the first application, tension stiffening was considered in the analysis of an RC cooling tower shell. For this example, con-

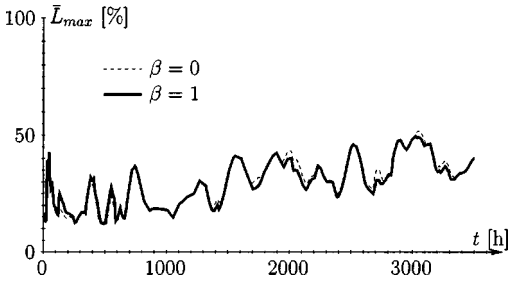

Fig. 22. Lainzer tunnel (km 8.340): evolution of $\overline{L}_{\max}$

sideration of tension stiffening resulted in a change of the load-carrying behavior and, hence, in a change of the failure mode. This was reflected by the significant increase of the collapse load as well as the corresponding deformations of the shell with increasing level of consideration of tension stiffening.

- Application of the proposed mode of consideration of the steel-concrete interaction in the context of hybrid analyses of shotcrete linings required the extension of the tension stiffening concept to early-age cracking. The underlying (aging) bond stress–bond slip relation was derived from experimental data taken from the open literature. In contrast to the analysis of the cooling tower, the displacements at the shotcrete lining were provided by the construction site. Accordingly, the change of stiffness in consequence of consideration of tension stiffening did not effect the deformations. This was the reason for the observed small influence of tension stiffening on the numerical results, especially on the level of loading of the lining.

The objectivity of the proposed approach for consideration of steel-concrete interaction with respect to the size of the finite elements was demonstrated by means of uniform and adaptive mesh refinement in previous publications. The reader is referred to Lackner and Mang (2001a, 2002a).

Notation

The following notation is used in this paper:

a_s = steel area per unit length;
c = concrete cover;
$d_{\max}$ = maximum aggregate size of concrete/shotcrete;
E_c = Young's modulus of concrete/shotcrete;
$E_{c,\infty}$ = Young's modulus of shotcrete at complete hydration;
E_s = Young's modulus of steel;
f_{cb} = biaxial compressive strength of concrete/shotcrete;
f_{cu} = uniaxial compressive strength of concrete/shotcrete;
$f_{cu,0}$ = reference value for uniaxial compressive strength of concrete/shotcrete;
$f_{cu,\infty}$ = uniaxial compressive strength of shotcrete at complete hydration;
f_{cy} = elastic limit of concrete/shotcrete under uniaxial compressive loading, with $f_{cy} = 0.4 f_{cu}$;
f_{D} = Drucker-Prager yield function;
f_{R} = Rankine yield function;
f_{sy} = yield stress of steel;
f_{tu} = uniaxial tensile strength of concrete/shotcrete;
G_c = shear modulus of concrete;
G^f = fracture energy of concrete/shotcrete;
G_0^f = reference value for fracture energy of concrete/shotcrete;
G_∞^f = fracture energy of shotcrete at complete hydration;
$h_{c,\mathrm{eff}}$ = effective tension height of concrete;
I_1 = first invariant of stress tensor;
J_2 = second invariant of stress deviator;
L = level of loading in tunnel lining analysis;
$\overline{L}$ = mean value of level of loading over lining thickness;
ℓ_k = length of kth layer of beam element in tunnel lining analysis;
ℓ_s = average crack spacing in reinforced concrete;
$\ell_{s,z}$ = average spacing between circumferential cracks in tunnel lining analysis;
$\ell_{s,\varphi}$ = average spacing between longitudinal cracks in tunnel lining analysis;
ℓ_s^{red} = *artificially-reduced* average crack spacing in reinforced concrete/shotcrete;
m = mass of water bound in hydrates;
m_∞ = mass of water bound in hydrates at complete hydration;
$\overline{\mathbf{n}}$ = vector perpendicular to inner surface of tunnel lining;
n_z = axial force in tunnel lining in longitudinal direction;
n_φ = axial force in tunnel lining in circumferential direction;
$\overline{q}$ = reference wind load in cooling tower analysis;
$\overline{q_{\mathrm{D}}}$ = compressive strength of concrete/shotcrete;
$\overline{q_{\mathrm{R}}}$ = tensile strength of concrete/shotcrete;
$\overline{q_{\mathrm{RF}}}$ = strength of steel;
$\overline{q_u}$ = reference wind load at collapse of cooling tower;
R = radius for description of tunnel cross section;
s = bond slip; circumferential coordinate in tunnel lining analysis;
s_1, s_2, s_3 = material parameters describing bond stress–bond slip relation;
t = thickness of cooling tower shell and tunnel lining;
$\mathbf{u}$ = displacement vector of an arbitrary point of shotcrete lining;
$\overline{\mathbf{u}}$ = displacement vector at inner surface of shotcrete lining;
$[\![u]\!]$ = crack width;
$[\![\overline{u}]\!]$ = reference crack width;
$\mathcal{W}^f$ = released energy in consequence of cracking;
x = horizontal coordinate in tunnel lining analysis;
x_3 = vertical Cartesian coordinate in cooling tower analysis;
y = vertical coordinate in tunnel lining analysis;
z = longitudinal coordinate in tunnel lining analysis;
α_{D} = internal variable of Drucker-Prager criterion;
α_{R} = internal variable of Rankine criterion;
α_{RF} = internal variable of plasticity criterion for steel;
$\overline{\alpha_{\mathrm{D}}}$ = calibration parameter of Drucker-Prager criterion;
$\overline{\alpha_{\mathrm{R}}}$ = calibration parameter of Rankine criterion;
β = dimensionless parameter for consideration of tension stiffening;
β_{D} = constant material parameter for Drucker-Prager criterion;

γ_D = plastic multiplier of Drucker-Prager criterion;
γ_R = plastic multiplier of Rankine criterion;
$\boldsymbol{\varepsilon}^p$ = tensor of plastic strains;
ε_φ = axial strain in circumferential direction of tunnel lining;
ε_z = axial strain in longitudinal direction of tunnel lining;
ε_1^p = principal plastic strain;
ε^u = total strain at peak stress of concrete/shotcrete under uniaxial compressive loading;
ζ = normalized radial coordinate in tunnel lining analysis;
Θ = circumferential angle for cooling tower analysis;
κ_D = constant material parameter for Drucker-Prager criterion;
ν_c = Poisson's ratio of concrete/shotcrete;
ξ = degree of hydration;
ρ_s = reinforcement ratio, given by $a_s/h_{c,\text{eff}}$;
$\boldsymbol{\sigma}$ = stress tensor;
σ = uniaxial stress employed in material model for steel;
σ_z = axial stress in longitudinal direction of tunnel lining;
σ_1, σ_2 = principal stresses in plane-stress model;
σ_φ = axial stress in circumferential direction of tunnel lining;
τ = bond stress;
$\tau_f, \tau_{\max}$ = material parameters describing bond stress–bond slip relation;
$\tau_{f,\infty}, \tau_{\max,\infty}$ = material parameters describing bond stress–bond slip relation at complete hydration; and
$\varnothing_s$ = diameter of reinforcement bar.

References

Bažant, Z. (1979). "Thermodynamics of solidifying or melting viscoelastic material." *J. Eng. Mech. Div., ASCE,* 105(6), 933–952.

Cedolin, L., and Poli, S. Dei (1977). "Finite element studies of shear-critical R/C beams." *J. Eng. Mech. Div., ASCE* 103(3), 395–410.

Chapman, R., and Shah, S. (1987). "Early-age bond strength in reinforced concrete." *ACI Mater. J.*, November–December, 501–510.

Comité Euro-International du Béton-Fédération International de la Précontrainte (CEB-FIP). (1990). *Model code 1990, bulletin d'information*. CEB, Lausanne, Switzerland.

De Schutter, G., and Taerwe, L. (1997). "Fracture energy of concrete at early ages." *Mater. Struct.*, 30, 67–71.

Floegl, H., and Mang, H. (1982). "Tension stiffening concept based on bond slip." *J. Struct. Div. ASCE,* 108(12), 2681–2701.

Hellmich, C., Mang, H., and Ulm, F.-J. (1999a). "Hybrid method for quantification of stress states in shotcrete tunnel shells: Combination of 3D *in-situ* displacement measurements and thermochemoplastic material law." *CD-ROM Proc., 1st European Conf. of Computational Mechanics*, W. Wunderlich, ed., Munich, Germany; also published in *Comput. Struct.,* 79, 2103–2115 (2001).

Hellmich, C., Ulm, F.-J., and Mang, H. A. (1999b). "Multisurface chemoplasticity. I: Material model for shotcrete." *J. Eng. Mech.,* 125(6), 692–701.

Lackner, R., Hellmich, C., and Mang, H. (2002). "Constitutive modeling of cementitious materials in the framework of chemoplasticity." *Int. J. Numer. Methods Eng.,* 53(10), 2357–2388.

Lackner, R., and Mang, H. (2001a). "Adaptive FE analysis of RC shells. II: Applications." *J. Eng. Mech.,* 127(12), 1213–1222.

Lackner, R., and Mang, H. (2001b). "Chemoplastic material model for the simulation of early-age cracking: From experiments to the constitutive law." *Proc., RILEM Int. Conf. on Early Age Cracking of Cementitious Systems*, K. Kovler and A. Bentur, eds., Haifa, Israel, 19–29.

Lackner, R., and Mang, H. (2001c). "Cracking in shotcrete tunnel shells." *Fracture Mechanics of Concrete Structures, Proc., 4th Int. Conf.*, R. de Borst, J. Mazars, G. Pijaudier-Cabor, and J. van Mier, eds., Cachan, France, 857–870; also published in *Eng. Frac. Mech.* 70(7–8), 1047–1068 (2003).

Lackner, R., and Mang, H. (2002a). "*A posteriori* error estimation in nonlinear FE analyses of shell structures." *Int. J. Numer. Methods Eng.,* 53(10), 2329–2355.

Lackner, R., and Mang, H. (2002b). "Modeling of early-age fracture of shotcrete: Application to tunneling." *Proc., IUTAM Symposium on Analytical and Computational Fracture Mechanics of Non-homogeneous Materials*, B. Karihaloo, ed., Cardiff, Wales, Kluwer Academic, Dordrecht, 197–210.

Lackner, R., and Mang, H. A. (2003). "Scale transition in steel-concrete interaction. I: Model." *J. Eng. Mech.,* 129(4), 393–402.

MARC (1996). *MARC reference manual-Volume B, element library*. MARC Analysis Research Corporation, Palo Alto, Calif. 94306. Multi-Purpose Finite Element Package.

Meschke, G. (1996). "Consideration of aging of shotcrete in the context of a 3D viscoplastic material model." *Int. J. Numer. Methods Eng.,* 39, 3123–3143.

Meschke, G., Huemer, Th., and Mang, H. (1999). "Computer-aided retrofitting of damaged RC cooling tower shell." *J. Struct. Eng.,* 125(3), 328–337.

Rokahr, R., and Zachow, R. (1997). "Ein neues Verfahren zur täglichen Kontrolle der Auslastung einer Spritzbetonschale (A new method for the daily monitoring of the stress intensity of a sprayed concrete lining)." *Felsbau,* 15(6), 430–434 (in German).

Ruetz, W. (1966). "Das Kriechen des Zementsteins im Beton und seine Beeinflussung durch gleichzeitiges Schwinden (Creep of cement in concrete as influenced by simultaneous shrinkage.)" Deutscher Ausschuß für Stahlbeton, Heft 183 (in German).

Sercombe, J., Hellmich, C., Ulm, F.-J., and Mang, H. A. (2000). "Modeling of early-age creep of shotcrete. I: Model and model parameters." *J. Eng. Mech.,* 126(3), 284–291.

Ulm, F.-J. (1998). "Couplages thermochémomécaniques dans les bétons: Un premier bilan. (Thermochemomechanical couplings in concretes: A first review)." *Technical Rep.*, Laboratoires des Ponts et Chaussées, Paris (in French).

Wittmann, F. (1982). *Creep and shrinkage mechanisms*, Wiley, Chichester, England, Chap. 6, 129–161.

Zachow, R. (1995). "Dimensionierung zweischaliger Tunnel in Fels auf der Grundlage von in-situ Messungen (Dimensioning of bicoque tunnels in rock masses based on in situ measurements)." *Technical Rep. 16*, Univ. of Hannover, Hannover, Germany (in German).